All-Optical Electrochemiluminescence

Yiran Zhao, Julie Descamps, Nour Al Hoda Al Bast, Marcos Duque, Jaume Esteve, Borja Sepulveda, Gabriel Loget, Néso Sojic

All-optical electrochemiluminescence

Yiran Zhao,[†] Julie Descamps,[‡] Nour al Hoda Al Bast,[§] Marcos Duque,[§] Jaume Esteve,[§] Borja Sepulveda,[§] Gabriel Loget,[†,∥,*] Neso Sojic[‡,*]

[†]Univ Rennes, CNRS, ISCR (Institut des Sciences Chimiques de Rennes)-UMR6226; Rennes, 35000, France.

[‡]University of Bordeaux, Bordeaux INP, ISM, UMR CNRS 5255; Pessac, 33607, France.

[§]Instituto de Microelectrónica de Barcelona (IMB-CNM, CSIC); Barcelona, 08193, Spain.

[∥]Institute of Energy and Climate Research, Fundamental Electrochemistry (IEK-9), Forschungszentrum Jülich GmbH; Jülich, 52425, Germany.

ABSTRACT: Electrochemiluminescence (ECL) is widely employed for medical diagnosis and imaging. Despite its remarkable analytical performances, the technique remains intrinsically limited by the essential need for an external power supply and electrical wires for electrode connections. Here, we report an electrically-autonomous solution leading to a paradigm change by designing a fully-integrated all-optical wireless monolithic photoelectrochemical device based on a nanostructured Si photovoltaic junction modified with catalytic coatings. Under illumination with light ranging from visible to near-infrared, photogenerated carriers induce the instantaneous oxidative emission of visible ECL photons. The blue ECL emission is easily viewed with naked eyes and recorded with a smartphone. A new light upconversion scheme is thus introduced where the ECL emission energy (2.82 eV) is higher than the excitation energy (1.18 eV) via an intermediate electrochemical process. In addition, the mapping of the photoelectrochemical activity by optical microscopy reveals the minority carrier interfacial transfer mechanism at the nanoscale. This breakthrough provides an all-optical strategy for generalizing ECL without the need for electrochemical setups, electrodes, wiring constraints, and specific electrochemical knowledge. This simplest ECL configuration reported so far opens new opportunities to develop imaging and wireless bioanalytical systems such as portable point-of-care sensing devices.

INTRODUCTION

Among the luminescence techniques, electrochemiluminescence (ECL) is an ultrasensitive analytical technique[1] that is widely applied in biosensing[2–4] and imaging.[5] The ECL light emission is triggered by electrochemistry.[6] The electrochemical reactions initiated at the electrode surface generate the excited state of the luminophore that relaxes by emitting light. Its intrinsic remarkable features are nicely exploited in biosensing, especially for clinical diagnostics with successfully commercialized immunoassays.[7–10] In addition, since ECL offers an optical readout, it evolves progressively from a pure analytical technique to a powerful microscopy.[11,12] For example, Feng et al. resolved spatially a single photon emitted by an individual ECL reaction.[5,13,14] Moreover, single entities such as nanoparticles, cells or mitochondria have been imaged by ECL microscopy.[15–22]

In spite of its exceptional analytical capabilities, ECL requires the use of an external source of electricity (typically, a potentiostat) powered by the local electrical network and an electrochemical setup involving reference and counter electrodes, connectors, and electrical wires. This considerably limits the applicability of ECL, especially for non-specialists and for on-site and portable analysis. In all the approaches documented so far, potentiostats or comparable electrical powering devices are necessary to produce ECL emission. Recent advances in photoinduced ECL have shown the possibility to reduce the potential needed to achieve ECL at an illuminated semiconductor electrode,[23–25] however external power sources were still required hitherto. Here, we report an original approach for true wireless ECL generation that only requires an all-integrated monolithic device and a light source. The approach, named all-optical ECL (AO-ECL), is based on a nanostructured *pnn*$^{++}$Si photovoltaic junction, modified with catalytic Au and Pt coatings to generate ECL and the associated counter reaction at each device side under illumination with a low-cost light-emitting diode. This electrically-autonomous strategy was inspired by research on monolithic water splitting photoelectrochemical devices,[26–35] in which the light absorbed by an immersed photovoltaic junction generates charge carriers that are directly employed at integrated catalytic interfaces for water electrolysis. It requires neither an electrical power supply nor additional electrodes, but only a single all-optical device im-

mersed in a standard ECL solution, thus constituting the simplest ECL configuration reported so far.

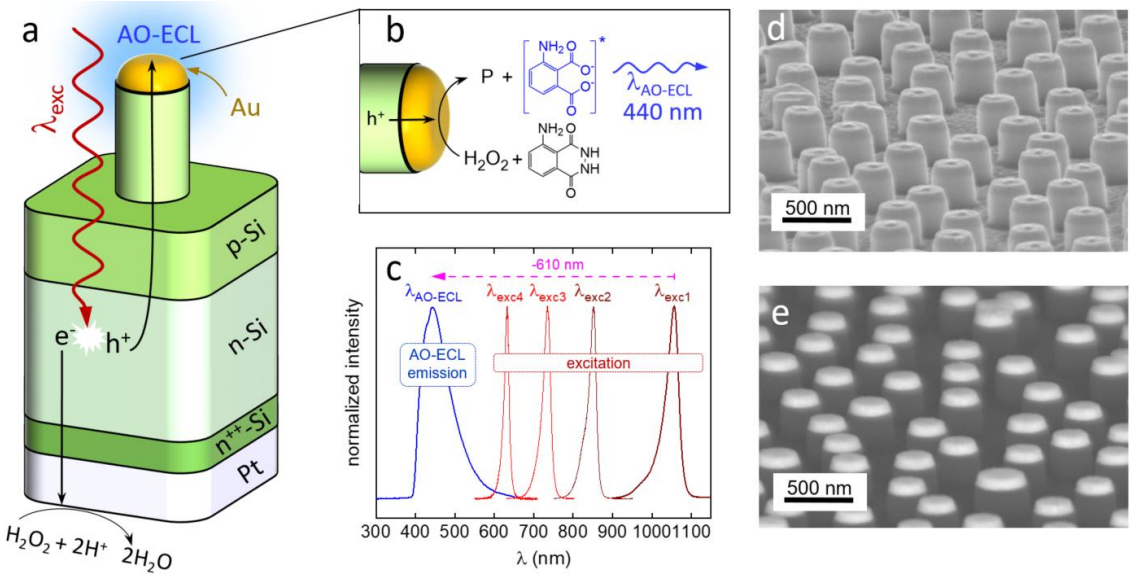

Figure 1. Description of the monolithic ECL device and light upconversion schemes. (a) Scheme of monolithic AO-ECL at a nanostructured Au-*pnn*$^{++}$Si-Pt junction under illumination. (b) Hole transfer mechanism leading to visible photons generation at the solid-liquid interface, P represents reaction products. (c) Normalized spectra of the incident excitation light emitting diodes (brown/red curves) and the resulting AO-ECL emission of luminol/H_2O_2 at Au-*pnn*$^{++}$Si-Pt (blue curve); the largest anti-Stokes shift is represented by a pink dashed arrow. (d and e) Secondary (d) and backscattered (e) electron microscopy images of the frontside of Au-*pnn*$^{++}$Si-Pt.

RESULTS AND DISCUSSION

The reported approach is based on photoelectrochemical Au-*pnn*$^{++}$Si-Pt devices that were manufactured on Si wafers by a combination of dopant implantation, nanosphere lithography, and reactive ion etching (Section *Manufacturing of the Au-pnn^{++}Si-Pt junction* in SI). As shown in Figure 1a, they are composed of a *pn*-Si photovoltaic junction interfaced at both sides with noble metal contacts, enabling efficient electrochemical reactions (Figure 1a,b). The implantation of a highly doped *n*$^{++}$Si layer between *n*Si and the Pt thin film (Figure S1) ensured the formation of an ohmic contact and optimal charge collection at the metal. The frontside (i.e., the illuminated side in Figure 1a) of the device comprised an array of randomly distributed Au-capped nanopillars with a diameter of ~275 nm and a total height of 265 nm, which comprises 190 nm of the silicon nanopillar and 75 nm of the Au nanodisk, as shown in Figure 1d (secondary electrons image), Figure 1e (backscattered electrons image) and Figure S2. X-ray photoelectron spectroscopy (XPS, Figure S3) confirmed the expected chemical composition at each side of the device (Section *Description of the XPS spectra* in SI) and scanning electron microscopy (SEM) revealed the geometry of the nanostructures at the frontside.Figure 1d-e show the entire nanopillars' morphology and the geometrical features of the Au nanodisks (a diameter of ~275 nm and a height of 75 nm). The nanopillars geometry was designed for operating from the visible to the near IR absorption and avoiding the shortcut of the *pn* junction when the electrolyte solution is exposed to both *n*- and *p*-doped regions. The Si-Au nanopillars exhibit enhanced absorption at 850 nm due to the excitation of a hybrid plasmonic-dielectric resonance (Figure S4a,c Section *Optical simulation* in SI). Note that the pure plasmonic resonance of the Au nanodisk is located at 1.5 μm, i.e., much higher than the silicon bandgap 1.1 μm (Figure S4b,d). Due to its electrocatalytic performance for the H_2O_2 reduction,[36] a 50 nm-thick Pt (Figure S1) thin film was deposited at the backside (i.e., the non-illuminated side in Figure 1a) of the junction. In our studies, the Au-*pnn*$^{++}$Si-Pt device was immersed in a standard ECL aqueous system containing 3-aminophthalhydrazide (i.e., luminol) as the luminophore and H_2O_2.[1] These reagents constitute a model ECL system widely used in different fields such as biosensing, forensic science, and imaging.[1,37] The mechanism for the wireless AO-ECL generation occurring at the monolithic Au-*pnn*$^{++}$Si-Pt device during frontside illumination is depicted in Figure 1a,b. Under irradiation with photons having a higher energy than the Si bandgap (i.e., λ_{exc} < 1.1 μm), electron/hole pairs are generated at the photoactive Si *pn* junction, as it was confirmed by the photovoltaic solid-state measurements in Figure S5. Driven by the induced photovoltage (band diagram presented in Figure S6), the photogenerated electrons diffuse to the Pt surface where they trigger the H_2O_2 reduction, and the holes

diffuse to the Au contacts where they afford simultaneous oxidation of H_2O_2 and luminol. The concomitant oxidation of H_2O_2 and luminol, depicted in Figure 1b, is a well-known ECL process that produces blue light through a bond-breaking mechanism where the 3-aminophthalate* excited-state relaxes to the ground state by emitting a photon at λ_{ECL} = 440 nm.[1] In the case of the Au-*pnn*$^{++}$Si-Pt device, the illumination leads to an anti-Stokes process where low energy photons (from 1.18 eV) are converted into high energy photons (2.82 eV), resulting in an anti-Stokes shift, which can be higher than 600 nm (Figure 1c). Such a large shift allows to easily separate illumination from the AO-ECL emission.

To understand the wireless AO-ECL processes, the electrochemical properties of the frontside (the Au-*pnn*$^{++}$Si photoanode) and the backside (the Pt cathode) were independently investigated in the presence of the ECL electrolyte using a conventional three-electrode setup (Section *Photoelectrochemical measurements* and Figure S7 in SI). We first discuss the photoanode behavior. The blue voltammogram of Figure 2a, recorded on the Au-*pnn*$^{++}$Si under intermittent 850 nm irradiation (power density P_{LED} = 5 mW cm^{-2}), displays a pronounced photoactivity, which is characterized by a negligible dark current, a high photocurrent generation under near IR irradiation (maximum current density, j_{max} = 1.5 mA cm^{-2}), and a low onset potential (-0.52 V vs Ag/AgCl, Figure S8a). This measurement demonstrates that the photogenerated holes efficiently participate in oxidation processes at the solid-liquid interface. As a comparison, an Au-free and flat *pn*Si junction studied in the same illumination conditions only produced a 30-fold lower photocurrent density (50 µA cm^{-2}) (Figure 2a, green curve), due to the poor hole transfer at the SiO_x interface impeding the electrochemical reactivity.[38–40] This effect reveals the essential role of the nanostructured Au metal contacts to promote an efficient interfacial Faradaic process by protecting the underlying Si from electrical passivation.[41–43]

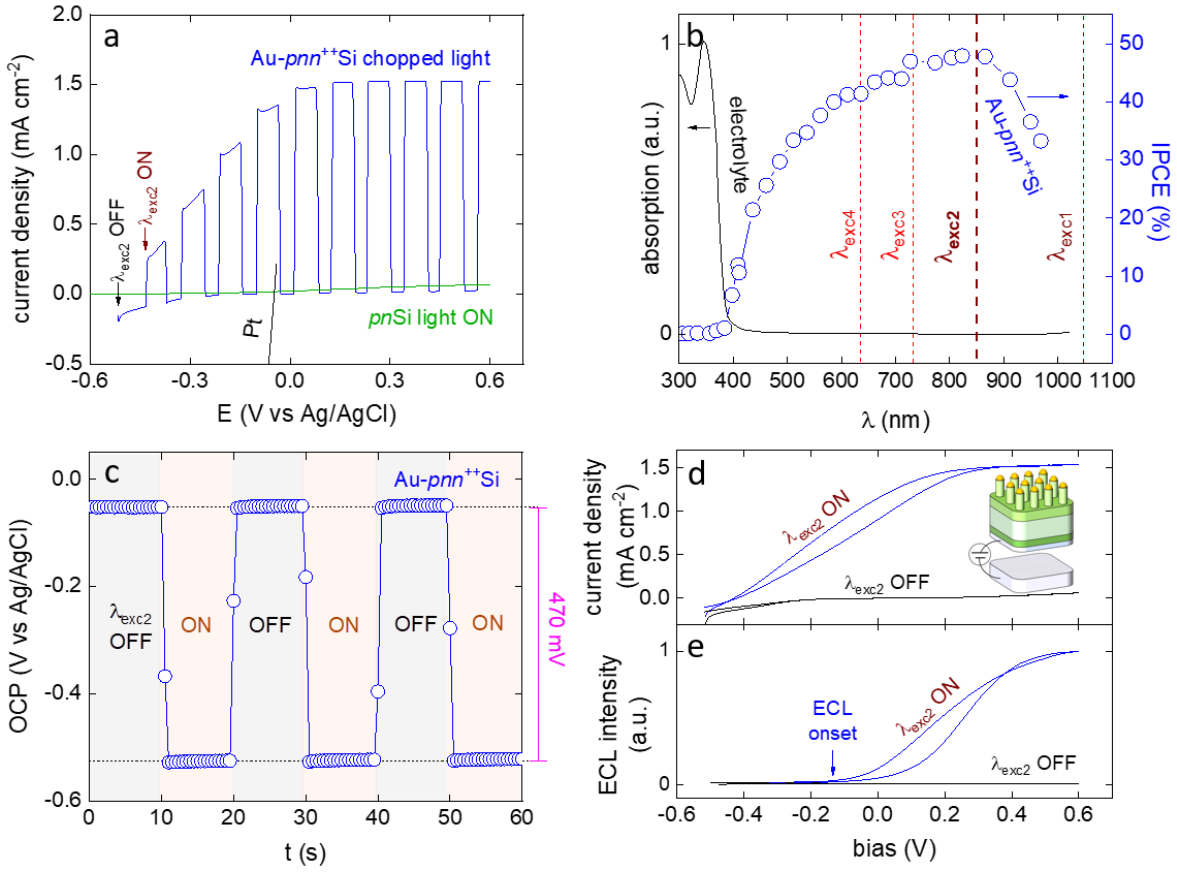

Figure 2. Electrochemical characterization of the involved surfaces. (a) Linear sweep voltammograms (50 mV s^{-1}) recorded with a three-electrode setup under intermittent IR light illumination at Au-*pnn*$^{++}$Si (blue curve), under illumination at *pn*Si (green curve), and in the dark at Pt (grey curve). (b) IPCE spectrum recorded with a three-electrode setup at Au-*pnn*$^{++}$Si (blue curve) at 0.6 V vs Ag/AgCl, overlaid with the electrolyte absorption (black curve). The excitation wavelengths are represented by dashed lines. (c) Open-circuit potential recorded with a three-electrode setup at Au-*pnn*$^{++}$Si under intermittent IR light illumination. The photovoltage is indicated by a pink line. (d and e) Cyclic voltammograms (50 mV s^{-1}) (d) and corresponding ECL intensity (e) measured with a two-electrode setup comprising an Au-*pnn*$^{++}$Si anode and a Pt cathode under IR light illumination (blue

curves) and in the dark (black curves). Inset: Scheme of the two-electrode setup. Electrolyte composition: 10 mM luminol, 33 mM H_2O_2 (pH = 12.8), 0.1% Triton X-100. λ_{exc2} = 850 nm, P_{LED} = 5 mW cm^{-2}.

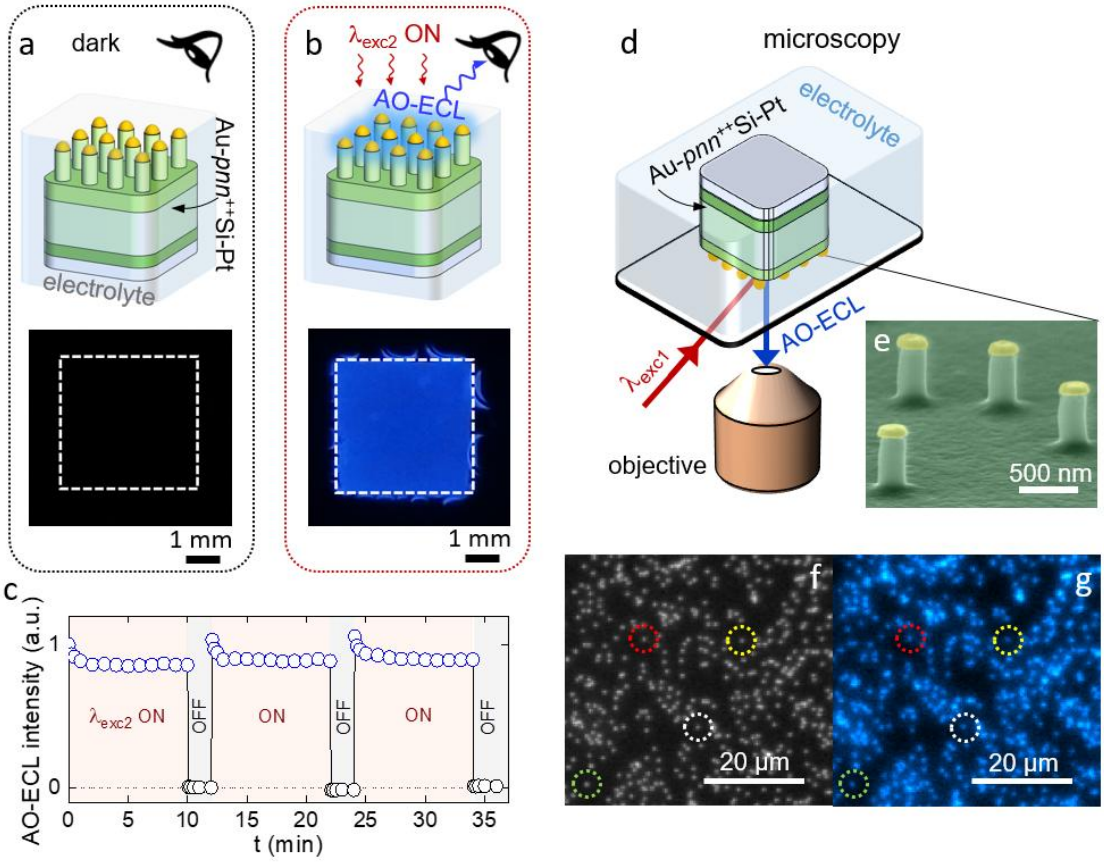

Figure 3. Monolithic photoelectrochemical upconversion resolved at the macroscopic and the single nanopillar scale. (a and b) Schemes (top) and corresponding smartphone photographs (bottom) showing Au-*pnn*$^{++}$Si-Pt immersed in the electrolyte in the dark (a) and under 850 nm illumination (b). (c) Graph showing the AO-ECL intensity emitted at Au-*pnn*$^{++}$Si-Pt frontside as a function of time under intermittent IR illumination (λ_{exc2} = 850 nm, P_{LED} = 18 mW cm^{-2}). (d) Scheme showing the ECL imaging setup. (e) Colored SEM image showing the Au-*pnn*$^{++}$Si-Pt frontside, structured with a low nanopillar density, studied by AO-ECL microscopy. (f and g) Optical microscopy images of the Au-*pnn*$^{++}$Si-Pt frontside (low nanopillar density) measured under white light (f) and IR (λ_{exc1} = 1050 nm, P_{LED} = 7 mW cm^{-2}) illumination (g). For clarity, four individual nanodisks are localized by colored dashed circles. Electrolyte composition: 10 mM luminol, 33 mM H_2O_2 (pH = 12.8), 0.1% Triton X-100.

The incident photon-to-current efficiency (IPCE) spectrum (Figure 2b, blue curve) recorded at 0.6 V vs Ag/AgCl at the Au-*pnn*$^{++}$Si confirmed the strong photoactivity of the electrode in the visible-to-near IR region with a maximum value of 48% at λ_{exc2} = 850 nm (note that the inactivity in the UV is caused by electrolyte absorption, Figure 2b, black curve). The open-circuit potential (OCP) measurements, performed under intermittent IR illumination, (Figure 2c), allowed measuring a photovoltage value of 0.47 V, which is in good agreement with the 0.46 V estimated by voltammetry (Figure S8b). On the other hand, the grey voltammogram of Figure 2a, recorded at the Pt thin film in the dark (i.e., the backside of the Au-*pnn*$^{++}$Si-Pt junction, Figure 1a), displays a cathodic activity at an onset potential of -0.07 V vs Ag/AgCl, corresponding to H_2O_2 reduction (a cyclic voltammogram study is provided in Figure S9). The fact that the cathode onset potential is more positive than that of the illuminated photoanode indicates that the two shorted electrodes (Au-*pnn*$^{++}$Si-Pt) should spontaneously generate photocurrent in this medium.

This behavior was tested using a two-electrode electrochemical setup (depicted in the inset of Figure 2d, details in Section *Photoelectrochemical measurements*, and Figure S10 in SI), which allows monitoring the current flow between the two surfaces as a function of bias. While negligible current was measured in the dark (Figure 2d, black curve), a considerable photocurrent was produced under the illumination of the Au-*pnn*$^{++}$Si photoanode with λ_{exc2} = 850 nm (Figure 2d, blue curve), with a short-circuit current density (i.e., at a bias of 0 V) of 1 mA cm^{-2}. If this proves that the system can spontaneously promote redox reactions at both faces, the possibility for AO-ECL generation was also assessed by measuring emission at the

photoanode with a spectrometer (details in Section *Photoelectrochemical measurements* and Figure S10a in SI). Figure 2e presents the ECL intensity signal recorded during the bias sweep and shows that ECL emission starts at negative bias, demonstrating the possibility for ECL generation in short-circuit conditions. This was further confirmed by monitoring the short-circuit ECL emission (Figure S11a,b present the setup and the control experiments, that are discussed in Section *Description of control experiments* in SI) as a function of time (Figure S11c) and P_{LED} (Figure S11d).

The Au-*pnn*$^{++}$Si-Pt monolithic device was then studied by immersing the entire surface in the ECL electrolyte without any contact and recording the blue light emission first with a smartphone camera (details in Section *Macroscale measurements of* AO-*ECL* and Figure S12 in SI). Indeed, the emitted AO-ECL light was bright enough to be easily viewed with naked eyes. As schematized in Figure 3a,b and demonstrated by the corresponding photographs, blue color light was observable only when λ_{exc2} = 850 nm was applied at the device frontside. The emission signal responded instantaneously to the IR stimulus, its intensity depended on the applied irradiation power density (Figure S13) and it was stable for 30 min without a decrease in intensity, as shown in Figure 3c. Similar behavior was observed with visible excitation (λ_{exc} = 733 and 633 nm, Figure S14). In other words, illumination wavelengths ranging from the visible to the near-IR can generate bright AO-ECL emission. The incident light can be conveniently tuned and the spectral limits are imposed at low and high wavelengths by the emission of the selected ECL system (to easily differentiate λ_{exc} from $\lambda_{AO\text{-}ECL}$) and the bandgap of Si, respectively. Finally, the phenomenon was investigated by microscopy experiments (depicted in Figure 3d, details in Section *Microscopy measurements of* AO-*ECL* and Figure S15 in SI) where the frontside of Au-*pnn*$^{++}$Si-Pt junctions, specifically tailored with a low density of nanopillars (Figure 3e and Figure S16), was observed under different illumination conditions. Under white light illumination, the gold-capped nanopillars appeared as white dots due to light reflection (Figure 3f). In contrast, under near IR illumination with λ_{exc1} = 1050 nm (Figure 3g), individual AO-ECL-emitting spots appeared, that colocalize with a good correlation with the white light image (Figure S17). The spatial distribution of AO-ECL emission spots (Figure 3g) matches perfectly the pattern observed by white light (Figure 3f). This experiment allowed the direct visualization of the upconversion process at the single nanopillar level (four randomly-chosen individual Si-Au nanopillars are identified by dotted circles in Figure 3f,g). In addition, this imaging approach demonstrates that the photogenerated solid-liquid charge transfer specifically occurs at the surface of the Au nanodisks, thereby enabling direct visualization of the photoelectrochemical activity, which is essential to optimize catalytic photoelectrodes.[44]

CONCLUSION

To conclude, our results highlight a novel all-optical strategy for the generation of ECL emission in a wireless manner without any electrical power supply, any electrochemical setups, any additional electrodes and the constraints related to the electrode connections. The ability to produce electrically-autonomous ECL using the simplest configuration reported so far is in marked contrast to current methods that are limited by the requirement of such specific electrochemical setups and knowledge. Using immersed Au-*pnn*$^{++}$Si-Pt fully-integrated monolithic devices, comprising a nanostructured photovoltaic junction interfaced with electroactive conductive coatings, we were able to directly exploit photogenerated carriers for wireless and stable ECL emission. In this process, the light absorption by the nanostructured surface triggers electrochemical activity, which, in turn, induces the generation of blue light ($\lambda_{AO\text{-}ECL}$ = 440 nm). This blue ECL was produced efficiently with excitation wavelengths ranging from the visible (633 nm) to the near IR (1050 nm). Microscopy experiments allowed us to correlate the emission spots with the nanoscale architecture of the device, demonstrating that interfacial charge transfer specifically occurs at the Au nanodisk-liquid interface. This process is remarkable in several aspects. As such, it constitutes an unprecedented direct upconversion process (among rare examples such as two-photon absorption or triplet-triplet annihilation)[45] working at low light intensities, where the emission energy (2.82 eV) is higher than the excitation energy (down to 1.18 eV). This represents an ultimate anti-Stokes shift of -610 nm. From an analytical point of view, although we have demonstrated it on these specifically tailored Au-*pnn*$^{++}$Si-Pt devices, this strategy should be also effective with other photoelectrochemical devices, such as nanostructured photoelectrodes,[46–48] semiconductor photocatalysts[49,50] or artificial leaves,[51,52] and can play a relevant role in elucidating energy conversion mechanisms at the nanoscale. Finally, due to its all-optical nature, the simplicity and versatility of the reported approach should extend this powerful technique to non-specialists. Given the importance of ECL technologies for biosensing and medical diagnosis,[1–3] this phenomenon has a strong potential for the development of a new generation of sensitive and portable biosensing devices and imaging strategies.

ASSOCIATED CONTENT

Supporting Information.
This material is available free of charge via the Internet at http://pubs.acs.org.

Experimental section and additional surface characterization, electrical and optical data.

AUTHOR INFORMATION

Corresponding Author

*gabriel.loget@cnrs.fr
*sojic@u-bordeaux.fr

Funding Sources

The research was funded by ANR (LiCORN - ANR-20-CE29-0006) and the Spanish Ministerio de Ciencia, Innovación y Universidades (MICINN) through the PID2019-106229RB-I00 and PCI2019-111896-2 (Euronanomed 2019) projects funded by MCIN/AEI/10.13039/501100011033.

Notes

The authors declare no competing interests.

ACKNOWLEDGMENT

Loic Joanny and Francis Gouttefangeas (ScanMat/CMEBA) are acknowledged for SEM. The XPS platform and Dr. Corinne Lagrost (Univ Rennes, CNRS, ScanMat), UAR2025, are acknowledged. Prof. Alexander Kuhn (Univ. Bordeaux, ISM), Prof. Francisco Javier del Campo (BCMaterials), Dr. Lionel Santinacci and Dr. Yoan Léger from CNRS are acknowledged for valuable discussions.

REFERENCES

(1) Liu, Z.; Qi, W.; Xu, G. Recent Advances in Electrochemiluminescence. *Chem. Soc. Rev.* **2015**, *44*, 3117–3142.
(2) Yang, H.; Leland, J. K.; Yost, D.; Massey, R. Electrochemiluminescence: A New Diagnostic and Research Tool. *Nat. Biotechnol.* **1994**, *12*, 193–194.
(3) Zanut, A.; Fiorani, A.; Canola, S.; Saito, T.; Ziebart, N.; Rapino, S.; Rebeccani, S.; Barbon, A.; Irie, T.; Josel, H.-P.; Negri, F.; Marcaccio, M.; Windfuhr, M.; Imai, K.; Valenti, G.; Paolucci, F. Insights into the Mechanism of Coreactant Electrochemiluminescence Facilitating Enhanced Bioanalytical Performance. *Nat. Commun.* **2020**, *11*, 2668.
(4) Ma, X.; Gao, W.; Du, F.; Yuan, F.; Yu, J.; Guan, Y.; Sojic, N.; Xu, G. Rational Design of Electrochemiluminescent Devices. *Acc. Chem. Res.* **2021**, *54*, 2936–2945.
(5) Dong, J.; Lu, Y.; Xu, Y.; Chen, F.; Yang, J.; Chen, Y.; Feng, J. Direct Imaging of Single-Molecule Electrochemical Reactions in Solution. *Nature* **2021**, 244–249.
(6) Ding, Z.; Quinn, B. M.; Haram, S. K.; Pell, L. E.; Korgel, B. A.; Bard, A. J. Electrochemistry and Electrogenerated Chemiluminescence from Silicon Nanocrystal Quantum Dots. *Science* **2002**, *296*, 1293–1297.
(7) Faatz, E.; Finke, A.; Josel, H.-P.; Prencipe, G.; Quint, S.; Windfuhr, M. Automated Immunoassays for the Detection of Biomarkers in Body Fluids. In *Analytical Electrogenerated Chemiluminescence: From Fundamentals to Bioassays*; The Royal Society of Chemistry: 2022; pp 443–470.
(8) Wang, Y.; Zhao, G.; Chi, H.; Yang, S.; Niu, Q.; Wu, D.; Cao, W.; Li, T.; Ma, H.; Wei, Q. Self-Luminescent Lanthanide Metal–Organic Frameworks as Signal Probes in Electrochemiluminescence Immunoassay. *J. Am. Chem. Soc.* **2021**, *143*, 504–512.
(9) Wang, Y.; Ding, J.; Zhou, P.; Liu, J.; Qiao, Z.; Yu, K.; Jiang, J.; Su, B. Electrochemiluminescence Distance and Reactivity of Coreactants Determine the Sensitivity of Bead-Based Immunoassays. *Angew. Chem. Int. Ed.* **2023**, *62*, e202216525.
(10) Zhu, W.; Dong, J.; Ruan, G.; Zhou, Y.; Feng, J. Quantitative Single-Molecule Electrochemiluminescence Bioassay. *Angew. Chem. Int. Ed.* **2023**, *62*, e202214419.
(11) Zhang, J.; Arbault, S.; Sojic, N.; Jiang, D. Electrochemiluminescence Imaging for Bioanalysis. *Annu. Rev. Anal. Chem.* **2019**, *12*, 275–295.
(12) Rebeccani, S.; Zanut, A.; Santo, C. I.; Valenti, G.; Paolucci, F. A Guide Inside Electrochemiluminescent Microscopy Mechanisms for Analytical Performance Improvement. *Anal. Chem.* **2022**, *94*, 336–348.
(13) Dong, J.; Xu, Y.; Zhang, Z.; Feng, J. Operando Imaging of Chemical Activity on Gold Plates with Single- Molecule Electrochemiluminescence Microscopy. *Angew. Chem. Int. Ed.* **2022**, *61*, e202200187.
(14) Zhou, Y.; Dong, J.; Zhao, P.; Zhang, J.; Zheng, M.; Feng, J. Imaging of Single Bacteria with Electrochemiluminescence Microscopy. *J. Am. Chem. Soc.* **2023**, *145*, 8947–8953.
(15) Zhao, W.; Chen, H.-Y.; Xu, J.-J. Electrogenerated Chemiluminescence Detection of Single Entities. *Chem. Sci.* **2021**, *12*, 5720–5736.
(16) Zhu, M.-J.; Pan, J.-B.; Wu, Z.-Q.; Gao, X.-Y.; Zhao, W.; Xia, X.-H.; Xu, J.-J.; Chen, H.-Y. Electrogenerated Chemiluminescence Imaging of Electrocatalysis at a Single Au/Pt Janus Nanoparticle. *Angew. Chem. Int. Ed.* **2018**, *130*, 4047–4078.
(17) Ding, H.; Guo, W.; Su, B. Imaging Cell-Matrix Adhesions and Collective Migration of Living Cells by Electrochemiluminescence Microscopy. *Angew. Chem. Int. Ed.* *59*, 449–456.
(18) Chen, M.-M.; Xu, C.-H.; Zhao, W.; Chen, H.-Y.; Xu, J.-J. Super-Resolution Electrogenerated Chemiluminescence Microscopy for Single-Nanocatalyst Imaging. *J. Am. Chem. Soc.* **2021**, *143*, 18511–18518.
(19) Valenti, G.; Scarabino, S.; Goudeau, B.; Lesch, A.; Jović, M.; Villani, E.; Sentic, M.; Rapino, S.; Arbault, S.; Paolucci, F.; Sojic, N. Single Cell Electrochemiluminescence Imaging: From the Proof-of-Concept to Disposable Device-Based Analysis. *J. Am. Chem. Soc.* **2017**, *139*, 16830–16837.
(20) Voci, S.; Goudeau, B.; Valenti, G.; Lesch, A.; Jović, M.; Rapino, S.; Paolucci, F.; Arbault, S.; Sojic, N. Surface-Confined Electrochemiluminescence Microscopy of Cell Membranes. *J. Am. Chem. Soc.* **2018**, *140*, 14753–14760.
(21) Liu, Y.; Zhang, H.; Li, B.; Liu, J.; Jiang, D.; Liu, B.; Sojic, N. Single Biomolecule Imaging by Electrochemiluminescence. *J. Am. Chem. Soc.* **2021**, *143*, 17910–17914.
(22) Descamps, J.; Colin, C.; Tessier, G.; Arbault, S.; Sojic, N. Ultrasensitive Imaging of Cells and Sub-Cellular Entities by Electrochemiluminescence. *Angew. Chem. Int. Ed.* **2023**, *62*, e202218574.
(23) Zhao, Y.; Yu, J.; Xu, G.; Sojic, N.; Loget, G. Photoinduced Electrochemiluminescence at Silicon Electrodes in Water. *J. Am. Chem. Soc.* **2019**, *141*, 13013–13016.
(24) Zhao, Y.; Descamps, J.; Ababou-Girard, S.; Bergamini, B.; Bergamini, L.; Léger, Y.; Sojic, N.; Loget, G. Metal-Insulator-Semiconductor Anodes For Ultrastable AndSiteSelective Upconversion Photoinduced Electrochemiluminescence. *Angew. Chem. Int. Ed.* **2022**, *61*, e202201865.
(25) Vogel, Y. B.; Darwish, N.; Ciampi, S. Spatiotemporal Control of Electrochemiluminescence Guided by a Visible Light Stimulus. *Cell Rep. Phys. Sci.* **2020**, *1*, 100107.
(26) Fujishima, A.; Honda, K. Electrochemical Photolysis of Water at a Semiconductor Electrode. *Nature* **1972**, *238*, 37–38.
(27) Prévot, M. S.; Sivula, K. Photoelectrochemical Tandem Cells for Solar Water Splitting. *J. Phys. Chem. C* **2013**, *117*, 17879–17893.

(28) Khaselev, O.; Turner, J. A. A Monolithic Photovoltaic Photoelectrochemical Device for Hydrogen Production via Water Splitting. *Science* **1998**, *280*, 425–427.
(29) Sun, K.; Liu, R.; Chen, Y.; Verlage, E.; Lewis, N. S.; Xiang, C. A Stabilized, Intrinsically Safe, 10% Efficient, Solar Driven Water-Splitting Cell Incorporating Earth-Abundant Electrocatalysts with Steady-State PH Gradients and Product Separation Enabled by a Bipolar Membrane. *Adv. Energy Mater.* **2016**, *6*, 1600379.
(30) Sivula, K.; Van De Krol, R. Semiconducting Materials for Photoelectrochemical Energy Conversion. *Nat. Rev. Mater.* **2016**, *1*, 15010.
(31) Wang, Y.; Schwartz, J.; Gim, J.; Hovden, R.; Mi, Z. Stable Unassisted Solar Water Splitting on Semiconductor Photocathodes Protected by Multifunctional GaN Nanostructures. *ACS Energy Lett.* **2019**, *4*, 1541–1548.
(32) Fu, H.-C.; Varadhan, P.; Lin, C.-H.; He, J.-H. Spontaneous Solar Water Splitting with Decoupling of Light Absorption and Electrocatalysis Using Silicon Back-Buried Junction. *Nat. Commun.* **2020**, *11*, 3930.
(33) Zhou, P.; Navid, I. A.; Ma, Y.; Xiao, Y.; Wang, P.; Ye, Z.; Zhou, B.; Sun, K.; Mi, Z. Solar-to-Hydrogen Efficiency of More than 9% in Photocatalytic Water Splitting. *Nature* **2023**, *613*, 66–70.
(34) Ager, J. W.; Shaner, M. R.; Walczak, K. A.; Sharp, I. D.; Ardo, S. Experimental Demonstrations of Spontaneous, Solar-Driven Photoelectrochemical Water Splitting. *Energy Environ. Sci.* **2015**, *8*, 2811–2824.
(35) Lewis, N. S.; Nocera, D. G. Powering the Planet: Chemical Challenges in Solar Energy Utilization. *Proc. Natl. Acad. Sci. U.S.A.* **2006**, *103*, 15729–15735.
(36) Katsounaros, I.; Mayrhofer, K. J. J. The Influence of Non-Covalent Interactions on the Hydrogen Peroxide Electrochemistry on Platinum in Alkaline Electrolytes. *Chem. Commun.* **2012**, *48*, 6660.
(37) Liu, Y.; Shen, W.; Li, Q.; Shu, J.; Gao, L.; Ma, M.; Wang, W.; Cui, H. Firefly-Mimicking Intensive and Long-Lasting Chemiluminescence Hydrogels. *Nat. Commun.* **2017**, *8*, 1003.
(38) Zhang, X. G. *Electrochemistry of Silicon and Its Oxide*; Kluwer Academic Publishers, 2007.
(39) Walter, M. G.; Warren, E. L.; McKone, J. R.; Boettcher, S. W.; Mi, Q.; Santori, E. A.; Lewis, N. S. Solar Water Splitting Cells. *Chem. Rev.* **2010**, *110*, 6446–6473.
(40) Bae, D.; Seger, B.; Vesborg, P. C. K.; Hansen, O.; Chorkendorff, I. Strategies for Stable Water Splitting via Protected Photoelectrodes. *Chem. Soc. Rev.* **2017**, *46*, 1933–1954.
(41) Hill, J. C.; Landers, A. T.; Switzer, J. A. An Electrodeposited Inhomogeneous Metal–Insulator–Semiconductor Junction for Efficient Photoelectrochemical Water Oxidation. *Nat. Mater.* **2015**, *14*, 1150–1155.
(42) Kenney, M. J.; Gong, M.; Li, Y.; Wu, J. Z.; Feng, J.; Lanza, M.; Dai, H. High-Performance Silicon Photoanodes Passivated with Ultrathin Nickel Films for Water Oxidation. *Science* **2013**, *342*, 836–840.
(43) Loget, G.; Mériadec, C.; Dorcet, V.; Fabre, B.; Vacher, A.; Fryars, S.; Ababou-Girard, S. Tailoring the Photoelectrochemistry of Catalytic Metal-Insulator-Semiconductor (MIS) Photoanodes by a Dissolution Method. *Nat. Commun.* **2019**, *10*, 3522.
(44) Sambur, J. B.; Chen, T.-Y.; Choudhary, E.; Chen, G.; Nissen, E. J.; Thomas, E. M.; Zou, N.; Chen, P. Sub-Particle Reaction and Photocurrent Mapping to Optimize Catalyst-Modified Photoanodes. *Nature* **2016**, *530*, 77–80.
(45) Zhu, X.; Su, Q.; Feng, W.; Li, F. Anti-Stokes Shift Luminescent Materials for Bio-Applications. *Chem. Soc. Rev.* **2017**, *46*, 1025–1039.
(46) Liu, C.; Tang, J.; Chen, H. M.; Liu, B.; Yang, P. A Fully Integrated Nanosystem of Semiconductor Nanowires for Direct Solar Water Splitting. *Nano Lett.* **2013**, *13*, 2989–2992.
(47) Laskowski, F. A. L.; Oener, S. Z.; Nellist, M. R.; Gordon, A. M.; Bain, D. C.; Fehrs, J. L.; Boettcher, S. W. Nanoscale Semiconductor/Catalyst Interfaces in Photoelectrochemistry. *Nat. Mater.* **2020**, *19*, 69–76.
(48) Fabre, B.; Loget, G. Silicon Photoelectrodes Prepared by Low-Cost Wet Methods for Solar Photoelectrocatalysis. *Acc. Mater. Res.* **2023**, *4*, 133–142.
(49) Takata, T.; Jiang, J.; Sakata, Y.; Nakabayashi, M.; Shibata, N.; Nandal, V.; Seki, K.; Hisatomi, T.; Domen, K. Photocatalytic Water Splitting with a Quantum Efficiency of Almost Unity. *Nature* **2020**, *581*, 411–414.
(50) Teitsworth, T. S.; Hill, D. J.; Litvin, S. R.; Ritchie, E. T.; Park, J.-S.; Custer, J. P.; Taggart, A. D.; Bottum, S. R.; Morley, S. E.; Kim, S.; McBride, J. R.; Atkin, J. M.; Cahoon, J. F. Water Splitting with Silicon p–i–n Superlattices Suspended in Solution. *Nature* **2023**, *614*, 270–274.
(51) Nocera, D. G. The Artificial Leaf. *Acc. Chem. Res.* **2012**, *45*, 767–776.
(52) Reece, S. Y.; Hamel, J. A.; Sung, K.; Jarvi, T. D.; Esswein, A. J.; Pijpers, J. J. H.; Nocera, D. G. Wireless Solar Water Splitting Using Silicon-Based Semiconductors and Earth-Abundant Catalysts. *Science* **2011**, *334*, 645–648.

TOC GRAPHIC

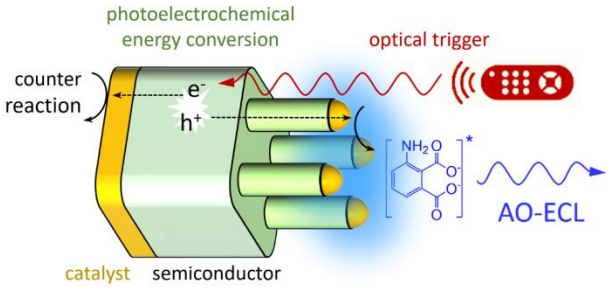
photoelectrochemical
energy conversion
optical trigger
counter
reaction
e-
h+
NH2
O
O-
O-
O
*
AO-ECL
catalyst
semiconductor